JOURNAL OF MATERIALS SCIENCE **40** (2005) 3059–3066

Atomic and electronic structure of [0001]/($\bar{1}\bar{2}$30) Σ7 symmetric tilt grain boundary in ZnO bicrystal with linear current-voltage characteristic

Y. SATO
Department of Advanced Materials Science, The University of Tokyo, 5-1-5 Kashiwanoha, Kashiwa, Chiba 277-8651, Japan

T. MIZOGUCHI, F. OBA*
Institute of Engineering Innovation, The University of Tokyo, 2-11-16 Yayoi, Bunkyo-ku, Tokyo 113-8656, Japan

M. YODOGAWA, T. YAMAMOTO‡
Department of Advanced Materials Science, The University of Tokyo, 5-1-5 Kashiwanoha, Kashiwa, Chiba 277-8651, Japan
E-mail: yamataka@k.u-tokyo.ac.jp

Y. IKUHARA
Institute of Engineering Innovation, The University of Tokyo, 2-11-16 Yayoi, Bunkyo-ku, Tokyo 113-8656, Japan

The atomic and electronic structures of [0001]/($\bar{1}\bar{2}$30) Σ7 symmetric tilt grain boundary in an undoped ZnO bicrystal were investigated by high-resolution transmission electron microscopy (HRTEM) and first-principles calculations. HRTEM imaging and atomistic calculations revealed that the grain boundary was composed of at least two types of structural units. It was also found that one of the structural units has two threefold-coordinated atoms per a unit and the other has two fivefold-coordinated atoms. First-principles calculations indicated that these atoms with various coordination numbers do not form deep unoccupied electronic states in the band gap of ZnO, which is in consistency with a linear current-voltage characteristic observed for the bicrystal with the Σ7 boundary.

1. Introduction

It is well known that grain boundaries (GBs) in polycrystals often dominate the electrical properties. In polycrystalline silicon used for solar cell and thin-film transistors, for example, GBs degrade the device performance [1–3]. On the other hand, GBs in electroceramics such as ZnO varistors and $BaTiO_3$ positive temperature coefficient of resistivity (PTCR) materials generate useful functions [4–9]. The GB effects on the electrical properties are often discussed in terms of double Schottky barriers (DSBs) formed at GBs.

The formation of DSB is closely related to GB atomic and electronic structures. DSB can be formed when deep electronic states appear in the band gap, and the appearance of the deep electronic states are dependent on the atomic structure and chemical composition. Altermatt *et al.* reported that electrical property across GBs in silicon significantly depends on the GB misorientations, i.e., atomic structures [2]. Kohyama *et al.* found that the electronic structures of silicon GBs depend on the atomic arrangements thus form deep electronic states in the band gap [10, 11]. In $BaTiO_3$, Hayashi *et al.* reported that highly coherent boundaries such as Σ3 and low angle GBs do not exhibit resistivity jumps while clear jumps are observed in incoherent GBs [8, 9].

ZnO polycrystals are well known to show highly nonlinear current-voltage (*I-V*) characteristics, when they are doped with certain impurities, such as Bi, Pr, and Co [5, 6, 12]. In this case, the atomic and electronic structures are influenced, by not only GB structure, but also the dopant type, and therefore these effects should be taken into account to consider the formation of DSB. It is thus necessary to quantitatively investigate the atomic and electronic structures of undoped and doped GBs in ZnO to reveal the origin of DSB [13–20]. Many papers reported that undoped GBs do not show nonlinear *I-V* characteristics [13, 14, 16, 17, 21, 23]. However, only one aspect (i.e., *I-V* characteristics, atomic structure, and electronic structure) was individually examined

* *Present address*: Department of Materials Science and Engineering, Kyoto University, Yoshida-Honmachi, Sakyo-ku, Kyoto 606-8501, Japan.
‡ Author to whom all correspondence should be addressed.

in each of previous paper. Therefore, it is important to investigate relationships between *I-V* characteristic, atomic structure, and electronic structure of the same GB in a comprehensive study, in order to understand the intrinsic properties of undoped ZnO GBs.

In the present study, the *I-V* characteristics, atomic structure, and electronic structure of the [0001]/($\bar{1}\bar{2}$30) Σ7 symmetric tilt GB (STGB) in undoped ZnO bicrystal were investigated by DC four-probe method, high-resolution transmission electron microscopy (HRTEM), and theoretical calculations. Detailed atomic structures of the GB were determined by experimental HRTEM observations in conjunction with atomistic calculations. The electronic structure of the determined atomic structures was also examined by first-principles calculations.

2. Experimental and computational procedures

2.1. Experimental procedure

Undoped ZnO bicrystal with the [0001]/($\bar{1}\bar{2}$30) Σ7 STGB was fabricated by hot-pressing two ZnO single crystals. The contact planes of two ZnO single crystals (purity: 99.99%, Earth Chemical. Co., Ltd.) were mechanochemically polished to a mirror state. They were jointed to preserve the Σ7 orientation, and annealed at 1100°C $\times$10 h in air under a uniaxial load of 1.5 MPa. The detailed fabrication procedure has been described elsewhere [21].

Several samples with the dimensions of 1.0 $\times$ 1.0 $\times$ 2.0 mm^3 were cut from the bicrystal and used for the *I-V* characteristic measurement and HRTEM observations. The *I-V* characteristic of the bicrystal was investigated by a DC four-probe method at room temperature in air, using a current source (Model 220, Keithley Instruments, Inc.) and a voltage meter (Model 2010, Keithley Instruments, Inc.). Ag-based paste was used as electrodes, which was confirmed to provide an Ohmic contact.

Thin foils for the TEM observations were prepared by a conventional method including mechanical polishing and dimpling down to about 20 μm and argon-ion-beam thinning with the accelerating voltage of 3–4 keV and beam angle of 12–15° (Duomill Model 600, Gatan, Inc.) to obtain an electron transparency. The GB was observed by using H-9000NAR operated at 300 kV (Hitachi Co., Ltd.).

2.2. Computational procedure

Atomistic calculations were also performed to investigate the GB atomic structures, in comparison with HRTEM images. Furthermore, the atomic structures were used for the first-principles band structure calculations to quantitatively examine their electronic structures.

GB atomic structures were modeled by the static lattice calculations with the GULP program code [24]. Buckingham type two-body ionic potentials were employed with the potential parameters reported by Lewis and Catlow [25]. These potential parameters can well reproduce both the experimental lattice constant and elastic constant of ZnO [14]. It was also confirmed that the GB atomic structures obtained by using these potential parameters are very close to that by the first principles calculation [13]. The static lattice calculations were made using supercells consisted of 76 to 80 atoms; supercells with smaller number of atoms than those used in our previous atomistic calculations [15] were employed so that the optimized structures can be applied to the electronic structure calculation.

HRTEM image simulations were performed using the obtained atomic structures by way of the Tempas program code based on the multi-slice methods [26]. HRTEM images were systematically simulated as a function of defocus and specimen thickness to yield an appropriate match with the experimental images.

Electronic structures were calculated using the first principles orthogonalized linear combinations of atomic orbital (OLCAO) method based on the density functional theory within the local density approximation (LDA) [27, 28]. The Bloch functions in the band structure calculation are constructed from the linear combination of atomic orbitals which are represented by a linear combination of a set of Gaussian-type orbitals. In the present study, a full basis function set consisting of atomic orbitals of Zn (1s, 2s, 2p, 3s, 3p, 3d, 4s, 4p, 4d, 5s, 5p) and O (1s, 2s, 2p, 3s, 3p) was employed for the self-consistent calculation. The core states were eliminated from the final secular equation by an orthogonalization process, which significantly reduces the computational time for large complex systems, such as GB. The number of *k*-points used in the irreducible portion of the Brillouin zone was two for the self-consistent calculation of all GB structures. The set of *k*-points was generated by the Monkhorst-Pack scheme with 1 $\times$ 1 $\times$ 3 mesh [29]. In the density of state (DOS) calculation, minimum basis function sets, namely 1s, 2s, 2p, 3s, 3p, 3d, 4s, 4p, 4d for Zn and 1s, 2s, 2p for O, were used to interpret the electronic structure in a simple manner. Sixty-four *k*-points were employed to obtain high resolution DOS, which was later broadened by both 0.1 and 0.01 eV via a Gaussian function.

3. Results and discussions

3.1. *I-V* characteristics and HRTEM observation

The obtained ZnO bicrystal exhibited a linear *I-V* characteristic as shown in Fig. 1. The resistivity of the bicrystal is about 26 Ω·cm, which is similar to that of ZnO single crystal perpendicular to [0001] (17 Ω·cm) that was subjected to annealing in the same condition as that for the bicrystal fabrication [22]. This indicates that two ZnO single crystals are perfectly joined.

Fig. 2 shows the HRTEM image of the same GB, indicating that the two ZnO single crystals are joined smoothly at the atomic level. The electron beam direction is parallel to the [0001] of both ZnO crystals, and both GB planes are ($\bar{1}\bar{2}$30). Judging from the diffraction

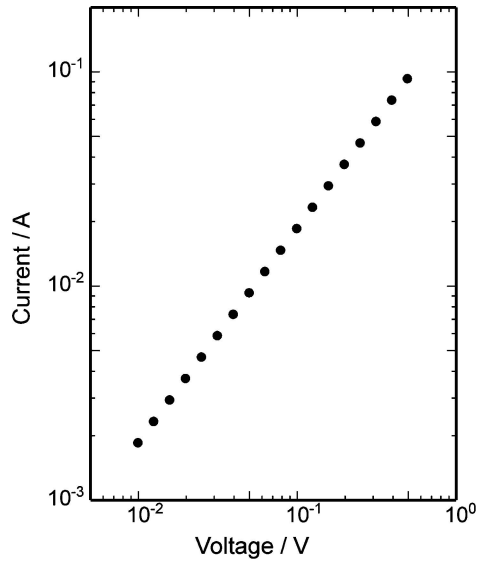

Figure 1 *I-V* characteristic of the ZnO bicrystal.

pattern shown in the inset, the misorientation angle between the axes in the adjacent crystals is about 22.0°. This indicates that the GB has the orientation relationship close to that of the ideal Σ7 orientation relationship (21.8°).

In detail, the GB was observed to have periodic structural units as illustrated by rhombuses (X and Y) in the figure. In addition, the structural units are likely to be classified into two types. Noticeable differences were observed between these two types of units. There are clear circular spots in the center of the unit X, and the spots at the right-hand corner are somewhat elongated and bent. On the contrary, the contrast of the center spots in the units Y is weak, and there are clear circular spots at the right-hand corner. In addition, the units X seem to be wider than Y in the direction of the boundary normal. These indicate that the GB contains at least two types of atomic structures.

TABLE I Energies of atomic structures of the {12$\bar{3}$0} Σ7 boundary obtained by atomistic calculations

Structure	Energy (Jm^{-2})
A	1.68
B	1.77
C	1.59

3.2. Atomic structure

Fig. 3 and Table I show the obtained atomic structures and the GB excess energies obtained by the present static lattice calculations. Three atomic structures, which will be denoted as A, B, and C, are selected from the same structures that were modeled in our previous study (corresponding to the structures B-D in Ref. 15). Although smaller supercells were employed in the present calculations, similar atomic positions and GB energies are found [15].

In structure A, there is a large open channel represented by a combination of fivefold- and sevenfold-coordinated channels (5/7-channels). This structure includes four threefold-coordinated atoms per unit GB area, 0.44 nm^{-2}. The shape of structure B resembles that of the structure A. However, the structure B has an additional atomic column in the center of 5/7-channels. As a result, only a smaller eightfold-coordinated open channel (8-channel) is left at the GB core. In addition, the number of the threefold-coordinated atoms decreased to two atoms per units. Structure C has a narrower GB core. Although this structure has no threefold-coordinated atoms, there are two fivefold-coordinated atoms per units. This fivefold-coordinated atomic column makes a very small fourfold-coordinated open channel (4-channel) with the other three atomic columns.

Fig. 4a–c show the simulated HRTEM images obtained from the atomic structures A-C. Among various defocuses and thicknesses, it was found that the

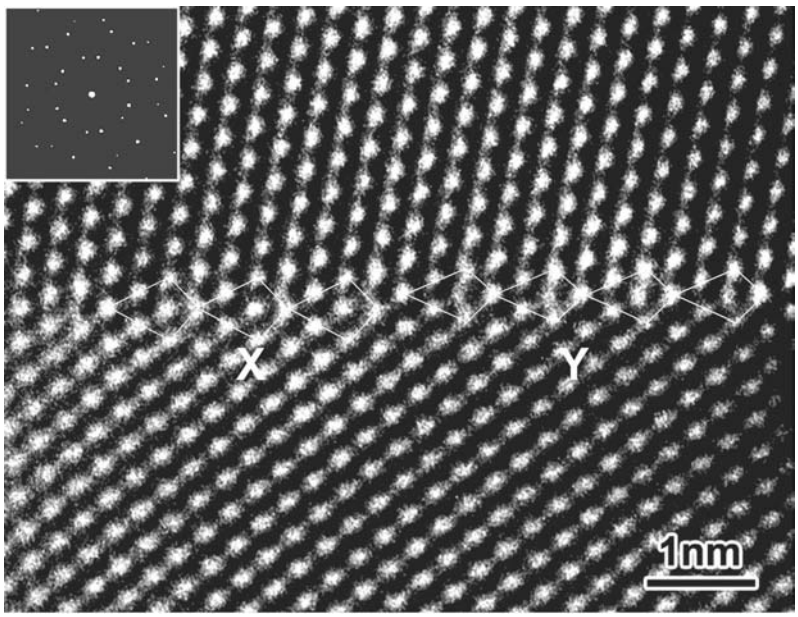

Figure 2 HRTEM image of the Σ7 [0001]/(1$\bar{2}$30) STGB in ZnO bicrystal. The inset shows a selected area diffraction pattern obtained from a region including both crystals.

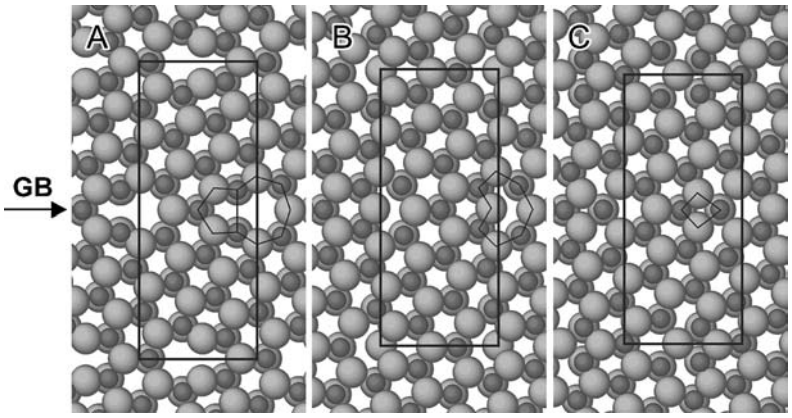

Figure 3 Atomic structures A-C of the $(\bar{1}\bar{2}30)$ Σ7 STGB calculated by static lattice calculations. The position of GB plane is indicated by the arrow. The smaller circles denote Zn and the larger ones denote O. The polygons show the 5/7-, 8-, and 4-channels, for structures A, B, and C, respectively. The rectangles denote supercells, i.e., periodicity units, used in the calculations.

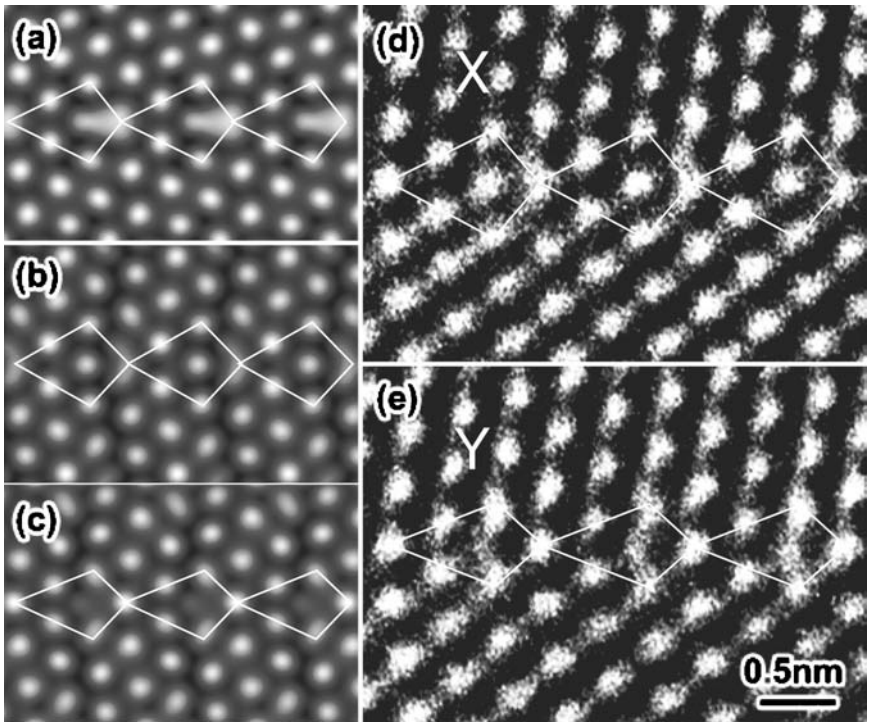

Figure 4 (a)–(c) Simulated HRTEM images for structures A–C with the defocus of −38 nm and the thickness of 4 nm. (d)–(e) Magnified HRTEM image of the units X and Y, respectively. White rhombuses show the structural units formed at GB cores.

simulated images of the structures B and C at 4 nm thickness and –38 nm defocus give the best agreement with the experimental HRTEM images. In this imaging condition, atomic positions appear dark and bright spot represents the location of an open channel.

Fig. 4d and e show magnified HRTEM images of the units X and Y in Fig. 3. Comparing with the simulated images in (a)–(c), it was found that the units X in the experimental image show very similar features to the simulated images of the structure B. The 8-channels in the structure B correspond to distorted bright spots at the right-hand corner of the units X and simulated image (b). In addition, the open channels next to 8-channels appeared as the clear circular spots in (b), which are also observed in (d). On the other hand, the units Y were found to show very similar feature, composed to the simulated image of the structure C. The 4-channels represent the darker spot in (c), and these are also observed in the experimental image (e). At the right-hand corner of the units, there are not distorted but clear circular spots next to the darker spots in both simulated image (c) and experimental image (e). Furthermore, the structural unit in (b) is wider than (c) in the direction of the boundary normal, which is also consistent with the difference between the units X and Y.

The agreement between experimental and simulated images was also confirmed at different imaging conditions. Fig. 5a and b show the experimental HRTEM images in the same areas as Fig. 4d and e, which were taken under a different defocus from the former ones. In this condition, HRTEM image simulations for the structures B and C give the best agreements at –70 nm defocus and 4 nm thickness as shown in Fig. 5c and d. The corner of the bright polygon approximately indicates the position of atoms. In both the units X in (a) and the structure B in (c), it was found that six atomic

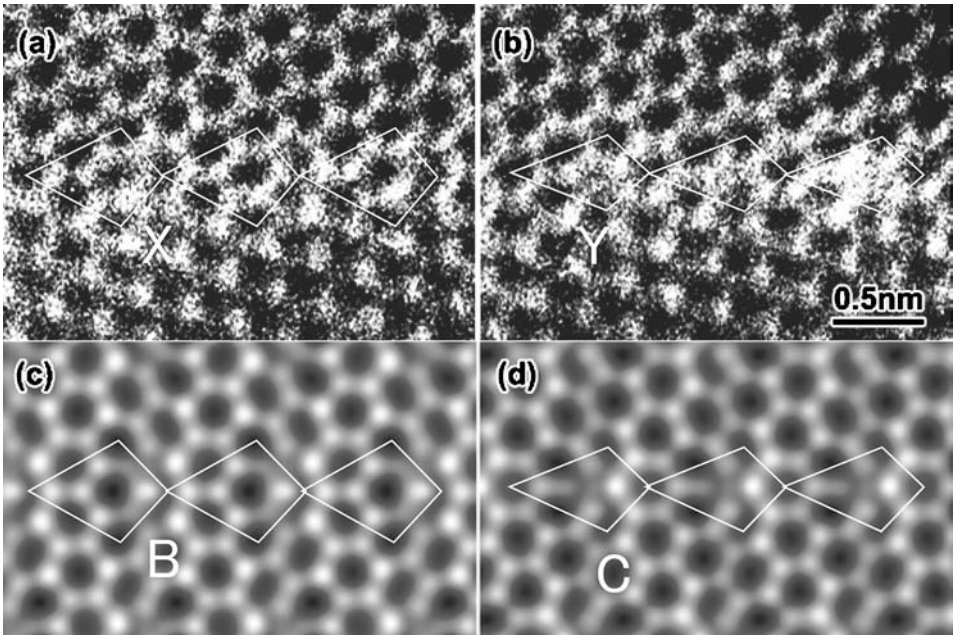

Figure 5 (a)–(b) Magnified HRTEM images obtained from the same areas as those in Fig. 4 (d) and (e). (c)–(d) Simulated HRTEM images for structures B-C with the defocus of −70 nm and the thickness of 4 nm. White rhombuses show the GB structural units.

columns make open channels at the center and distorted 8-channels at the right-hand corner. On the other hand, very small 4-channels are clearly found at the center of the units Y in (b) and the structure C in (d). In addition, there are clear circular dark spots at the right-hand corner in both (b) and (d). The structures B and C were, therefore, used as input for first-principles calculations to investigate the electronic structures. This will be discussed in the next section.

The structures A-C are very similar to those observed/calculated in GaN GBs/edge dislocations with the same wurtzite structure [29–33]. For edge dislocations in GaN, three structures were reported as stable structures with similar excess energies [30]. The structures contain the 5/7-, 8-, and 4-channels, respectively, and these can correspond to the GB structures A, B, and C in the present study. For GBs, Potin *et al.* reported that [0001]/($\bar{1}\bar{2}30$) $\Sigma 7$ STGBs in GaN films, which is the same orientation relationship as the present GB, were composed of the two structures corresponding to the present structures A and B [31]. On the other hand, Béré and Serra simulated that the structure with the 5/7-channel showed lowest GB excess energy for the same GB, which corresponds to the present structure A [32]. Concerning GBs and edge dislocations in ZnO, structures B and C were mainly observed in our previous HRTEM study of [0001] fiber-textured thin films [15]. In the present ZnO bicrystal, only two structures, B and C, were observed as in the case of thin films. The dominant structures for GBs and edge dislocations are thus considered to be different for GaN and ZnO.

3.3. Electronic structure

Left and right columns in Fig. 6 show the density of states (DOS) obtained from structures B and C, respectively. In order to examine the differences in the electronic structures between the GB and the bulk region, the total DOS is divided to two local DOS (LDOS). The first one is LDOS at GB (GB-LDOS), which is obtained by the sum of LDOS for the atomic columns labeled with **G** in the figures. The other one is LDOS from inter-GB regions denoted as quasi-bulk regions (QB-LDOS). The sources for the QB-LDOS are labeled with **Q**. GB and QB regions have 36 and 40 atoms, respectively for both structures. For comparison, DOS for the ZnO perfect crystal, which are normalized by the number of atoms, are also plotted by the dotted line in the figures. The top of the valence band for ZnO perfect crystal is chosen as 0 eV, and all LDOS are shifted to align the average of the lower valence band in the QB-region with that for ZnO perfect crystal. The calculated band gap of the ZnO perfect crystal is 1.3 eV, which is quite smaller than the experimental one of 3.3 eV in ZnO [35]. The disagreement is well known as an error associated with the LDA or GGA (generalized gradient approximation) [36, 37]. In order to avoid taking the error into consideration, only relative intensity and position of band-edge states are discussed in the present study.

Although the shape and the proportion of respective peaks are somewhat different, main features in all of DOS seem to be common. The lower valence band (VB) is formed at −17 eV, which is mainly composed of O-2s band. On the other hand, there is an upper valence band between −7.5 and 0 eV consisting of Zn-3d and O-2p bands. Above the band gap, unoccupied conduction band (CB) is formed by mainly Zn-4s, 4p, and 4d.

The band gaps in GB-LDOS and QB-LDOS of both structures are found to be approximately 0.8 eV, which is slightly smaller than that of the ZnO perfect crystal. Comparing to the DOS of ZnO, it is found that both conduction band (CB) and valence band (VB) edges invade to the band gap in both QB- and GB-LDOS. Therefore, the smaller band gap in QB- and GB-LDOS can be ascribed to broadenings of VB and CB, as also reported by

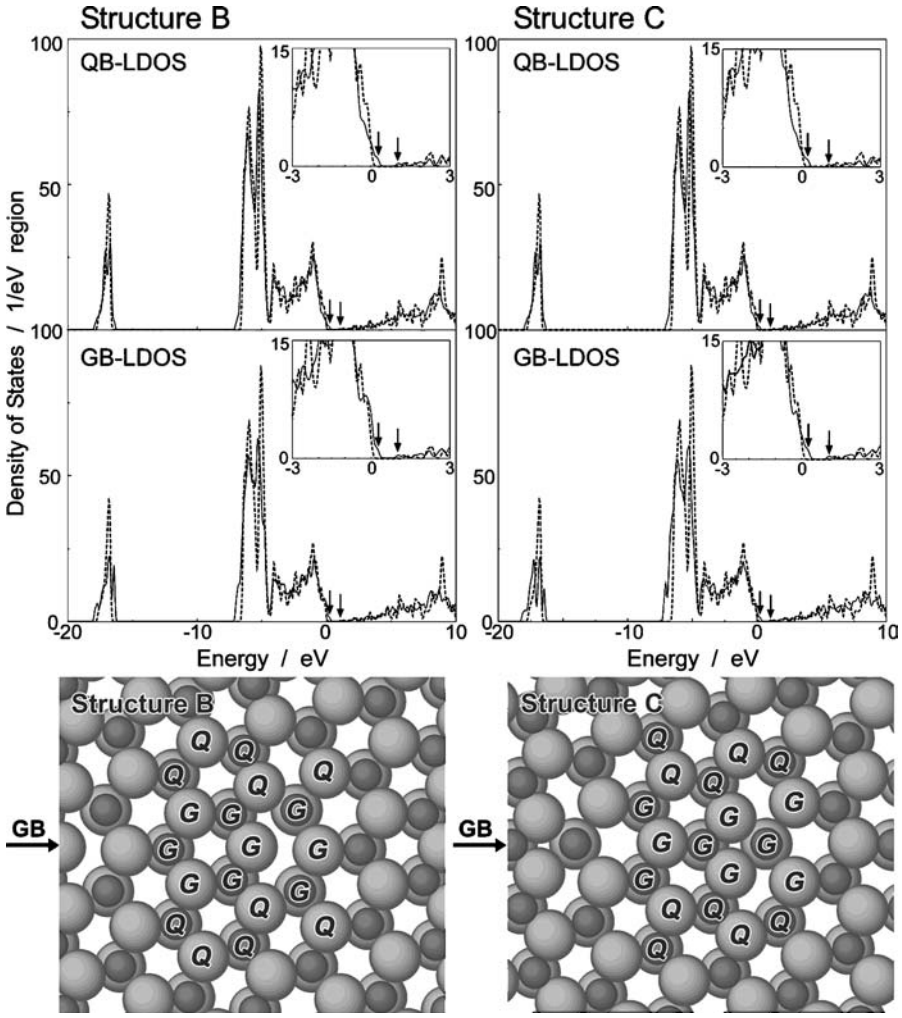

Figure 6 LDOS from GB and quasi-bulk (QB) regions for the structure B (left) and C (right). CB and VB edges in QB- and GB-LDOS are indicated by the arrows. For comparison, DOS for the ZnO perfect crystal is also shown by dotted line. Atomic columns in both structures are classified into GB and QB regions. In the lower figures, QB and GB regions are labeled with **G** and **Q**, respectively.

Domingos *et al.* at a [0001] Σ7 twist GB [17]. Because no defects and dopants are introduced in the present calculations, those broadenings are considered to originate from distorted and/or dangling bonds. Although the band gap becomes smaller due to the band broadening, no deep unoccupied states are formed in the band gap. Namely, it can be concluded that those band broadenings observed in the present structures do not become the origin of DSB. This is consistent with the linear *I*-*V* characteristic of this GB as shown in Fig. 1.

In order to examine the origin of the band broadening, DOS with a finer full width at half maximum of 0.01 eV are again divided into three LDOS. All of the LDOS are shifted in a similar manner to that of previous figures. As shown in right figures in Figs 7 and 8, atomic columns are classified into three kinds labeled with **H**, **J**, and **K**. For both structures, **H**, **J**, and **K** contain 2, 26, and 48 atoms, respectively. Although the ions in **J** and **K** are always fourfold-coordination, the atomic column labeled **H** exhibits various coordination; under-coordination (threefold-coordination) in structure B and over-coordination (fivefold-coordination) in structure C.

In the structure B, it is clearly found that the LDOS for the atomic column **H** exhibits intense peaks in the vicinity of VB edges. This indicates that the dangling bond at the GB core causes the VB broadening in structure B. It is interesting that such peaks at VB edges are also observed in the LDOS of the region **J**, whereas they are almost negligible in the LDOS for the region **K**. It is, therefore, likely that not only dangling bonds at the atomic column **H** but also distorted bonds in the region **J** result in the band broadening at the VB edge. In addition, the band broadening seems to be localized within two atomic layers of the GB.

On the other hand, the band broadening at VB edge does not occur in the atomic column **H** for structure C. The LDOS for the atomic column **H** in Fig. 8 does not exhibit remarkable peaks at the VB edges. Those peaks are, however, observed at the LDOS for the region **J**. Since there are no dangling/excess bonds in the region **J**, the band broadening can, again, be attributed to distorted bonds in this region. The directional localization of the band broadenings as found in structure B is also observed in structure C. As can be seen in Fig. 8, peaks at the VB edges are localized only at the region **J**, which includes two atomic layers perpendicular to the GB plane. Conversely, there are no peaks in the atomic column **H** and the region **K**.

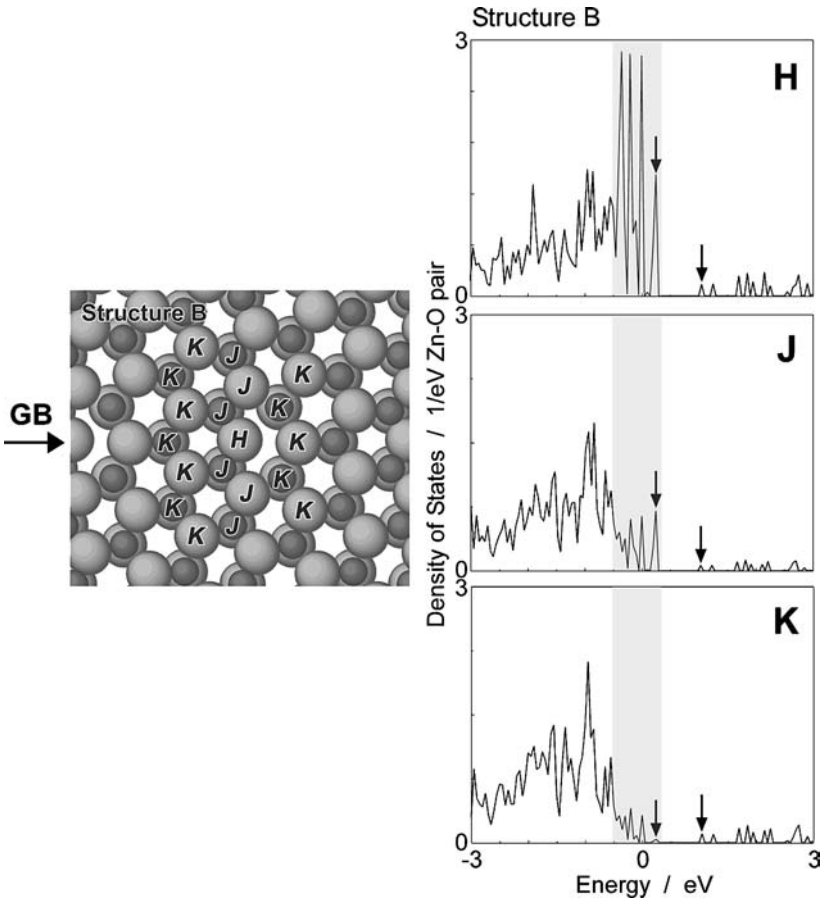

Figure 7 Enlarged LDOS from specific regions (**H**, **J**, and **K**) in the structure B. Atomic columns are classified into respective regions as shown in the left figure. All DOS are normalized by the number of the atoms. CB and VB edges are indicated by the arrows, and the area where VB broadenings appear are shown by the shaded region.

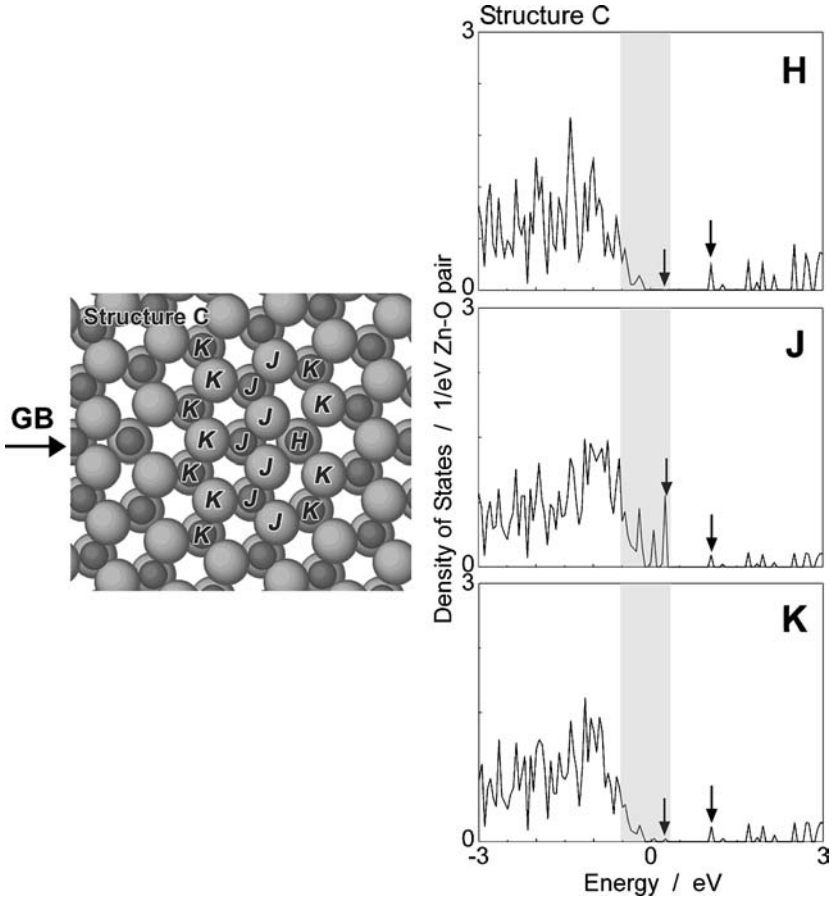

Figure 8 Enlarged LDOS from specific regions (**H**, **J**, and **K**) in the structure C. All DOS are normalized by the number of the atoms. CB and VB edges are indicated by the arrows, and the area where VB broadenings appear are shown by the shaded region.

4. Conclusions

The atomic and electronic structures of ZnO [0001]/($\bar{1}\bar{2}30$) $\Sigma 7$ STGB were investigated using HRTEM and theoretical calculations. HRTEM observation and atomistic calculation revealed that the GB contains two types of atomic structures. It was also found that one of them has an 8-channel, as well as threefold-coordinated atoms, at the GB core and the other has a 4-channel with fivefold-coordinated atoms at the GB core.

First-principles calculations revealed that these structures do not form have deep unoccupied electronic states in the band gap of ZnO, although the band broadening appears in the valence band and conduction band edge. This is believed to be the reason why this GB shows a linear I-V characteristic.

Acknowledgements

We thank Dr. J. D. Gale and Dr. W. Y. Ching for allowing us to use the GULP and OLCAO program codes, respectively. This work was supported by a Grant-in-Aid for Scientific Research and Special Coordination Funds from the Ministry of Education, Culture, Sports, Science and Technology of Japan. Two of the authors (YS and TM) also thank the Japan Society for the Promotion of Science for the research fellowship.

References

1. M. KOHYAMA, *Model. Simul. Mater. Sci. Eng.* **10** (2002) R31.
2. P. P. ALTERMATT and G. HEISER, *J. Appl. Phys.* **92** (2002) 2561.
3. J. W. TRINGE and J. D. PLUMMER, *ibid.* **87** (2000) 7913.
4. D. R. CLARKE, *J. Am. Ceram. Soc.* **82** (1999) 485.
5. M. MATSUOKA, *Jpn. J. Appl. Phys.* **10** (1971) 736.
6. K. MUKAE, K. TSUDA and I. NAGASAWA, *ibid.* **16** (1977) 1361.
7. W. HEYWANG, *J. Am. Ceram. Soc.* **47** (1964) 484.
8. K. HAYASHI, T. YAMAMOTO and T. SAKUMA, *ibid.* **79** (1996) 1669.
9. K. HAYASHI, T. YAMAMOTO, Y. IKUHARA and T. SAKUMA, *J. Appl. Phys.* **86** (1999) 2909.
10. M. KOHYAMA and R. YAMAMOTO, *Phys. Rev. B* **49** (1994) 17102 .
11. *Idem.*, *ibid.* **50** (1994) 8502.
12. M. YODOGAWA, Y. IKUHARA, F. OBA and I. TANAKA, *Key Eng. Mater.* **157/158** (1999) 249.
13. F. OBA, S. R. NISHITANI, H. ADACHI, I. TANAKA, M. KOHYAMA and S. TANAKA, *Phys. Rev. B.* **63** (2001) 045410-1.
14. F. OBA, I. TANAKA, S. R. NISHITANI, H. ADACHI, B. SLATER and D. H. GAY, *Philos. Mag. A* **80** (2000) 1567.
15. F. OBA, H. OHTA, Y. SATO, H. HOSONO, T. YAMAMOTO and Y. IKUHARA, *Phys. Rev. B.* (in press).
16. J. M. CARLSSON, B. HELLSING, H. S. DOMINGOS and P. D. BRISTOWE, *J. Phys: Condens. Matter* **13** (2001) 9937.
17. H. S. DOMINGOS and P. D. BRISTOWE, *Comput. Mater. Sci.* **22**(1) (2001) 38.
18. J. M. CARLSSON, H. S. DOMINGOS, B. HELLSING and P. D. BRISTOWE, *Interf. Sci.* **9** (2001) 143.
19. A. KISELEV, F. SARRAZIT, E. STEPANTSOV, E. OLSSON, T. CLASON, V. BONDARENKO, R. POND and N. KISELEV, *Philos. Mag. A* **76** (1997) 633.
20. J. M. CARLSSON, H. S. DOMINGOS, P. D. BRISTOWE and B. HELLSING, *Phys. Rev. Lett.* **91** (2003) 165506.
21. Y. SATO, F. OBA, T. YAMAMOTO, Y. IKUHARA and T. SAKUMA, *J. Am. Ceram. Soc.* **85** (2002) 2142.
22. Y. SATO, T. TANAKA, F. OBA, T. YAMAMOTO, Y. IKUHARA and T. SAKUMA, *Sci. Technol. Adv. Mater.* **4** (2003) 605.
23. N. OHASHI, Y. TERADA, T. OHGAKI, S. TANAKA, T. TSURUMI, O. FUKUNAGA, H. HANEDA and J. TANAKA, *Jpn. J. Appl. Phys. Part 1* **38** (1999) 5028.
24. J. D. GALE, *J. Chem. Soc. Faraday Trans.* **93** (1997) 629.
25. G. V. LEWIS and C. R. A. CATLOW, *J. Phys. C: Solid State Phys.* **18** (1985) 1149.
26. J. M. COWLEY and A. F. MOODIE, *Acta Cryst.* **10** (1957) 609.
27. W. Y. CHING, *J. Am. Ceram. Soc.* **73** (1990) 3135.
28. J. P. PERDEW and A. ZUNGER, *Phys. Rev. B* **23** (1981) 5048.
29. H. J. MONKHORST and J. D. PACK, *ibid.* **13** (1976) 5188.
30. A. BÉRÉ and A. SERRA, *ibid.* **66** (2002) 205323.
31. V. POTIN, P. RUTERANA, G. NOUET, R. C. POND and H. MORKOÇ, *ibid.* **61** (2000) 5587.
32. A. BÉRÉ and A. SERRA, *ibid.* **65** (2002) 085330.
33. J. CHEN, P. RUTERANA and G. NOUET, *Mater. Sci. Eng. B* **82** (2001) 117.
34. Y. XIN, S. J. PENNYCOOK, N. D. BROWNING, P. D. NELLIST, S. SIVANANTHAN, F. OMNÉS, B. BEAUMONT, J. P. FAURIE and P. GIBART, *Appl. Phys. Lett.* **72** (1998) 2680.
35. V. SRIKANT and D. R. CLARKE, *J. Appl. Phys.* **83** (1998) 5447.
36. P. SCHRÖER, P. KRÜGER and J. POLLMANN, *Phys. Rev. B* **47** (1993) 6971.
37. *Idem.*, *ibid.* **54**, 5495 (1996).

Received 29 July 2004
and accepted 31 January 2005